ADVANCED PHYSICS RESEARCH Open Access
www.advphysicsres.com

Large Enhancements in Optical and Piezoelectric Properties in Ferroelectric $Zn_{1-x}Mg_xO$ Thin Films through Engineering Electronic and Ionic Anharmonicities

*Rui Zu, Gyunghyun Ryu, Kyle P. Kelley, Steven M. Baksa, Leonard C. Jacques, Bo Wang, Kevin Ferri, Jingyang He, Long-Qing Chen, Ismaila Dabo, Susan Trolier-McKinstry, Jon-Paul Maria, and Venkatraman Gopalan**

Multifunctionality as a paradigm requires materials exhibiting multiple superior properties. Integrating second-order optical nonlinearity and large bandgap with piezoelectricity can, for example, enable broadband, strain-tunable photonics. Though very different phenomena at distinct frequencies, both second-order optical nonlinearity and piezoelectricity are third-rank polar tensors present only in acentric crystal structures. However, simultaneously enhancing both phenomena is highly challenging since it involves competing effects with tradeoffs. Recently, a large switchable ferroelectric polarization of ≈80 $\mu C\ cm^{-2}$ was reported in $Zn_{1-x}Mg_xO$ films. Here, ferroelectric $Zn_{1-x}Mg_xO$ is demonstrated to be a platform that hosts simultaneously a 30% increase in the electronic bandgap, a 50% enhancement in the second harmonic generation (SHG) coefficients, and a near 200% improvement in the piezoelectric coefficients over pure ZnO. These enhancements are shown to be due to a 400% increase in the electronic anharmonicity and a ≈200% decrease in the ionic anharmonicity with Mg substitution. Precisely controllable periodic ferroelectric domain gratings are demonstrated down to 800 nm domain width, enabling ultraviolet quasi-phase-matched optical harmonic generation as well as domain-engineered piezoelectric devices.

1. Introduction

The idea of fully integrated strain-tunable optical devices such as adaptive optics, strain tunable photonic crystals, and phase-matched nonlinear optical (NLO) conversion devices requires the integration of piezoelectric and optical materials.[1–8] A single multifunctional material that could achieve both effective strain tuning of materials properties and exceptional optical response would be ideal from an engineering design perspective, but relatively few candidates are known, and of these, many are limited to bulk single crystals.[9,10]

Both piezoelectricity and optical second harmonic generation (SHG), the subjects of this study, are third-rank tensor properties with the same tensor form; both require acentric structures with broken spatial inversion symmetry. Since the most direct way to break inversion symmetry is in a polar structure with

R. Zu, G. Ryu, S. M. Baksa, B. Wang, K. Ferri, J. He, L.-Q. Chen, I. Dabo, S. Trolier-McKinstry, J.-P. Maria, V. Gopalan
Department of Materials Science and Engineering
The Pennsylvania State University
University Park
PA 16802, USA
E-mail: vxg8@psu.edu

K. P. Kelley
Center for Nanophase Materials Sciences
Oak Ridge National Laboratory
Oak Ridge, TN 37831, USA

L. C. Jacques, L.-Q. Chen, V. Gopalan
Department of Engineering Science and Mechanics
The Pennsylvania State University
University Park
PA 16802, USA

L.-Q. Chen
Department of Mathematics
The Pennsylvania State University
University Park
PA 16802, USA

S. Trolier-McKinstry, V. Gopalan
Materials Research Institute
The Pennsylvania State University
University Park
PA 16802, USA

V. Gopalan
Department of Physics
Pennsylvania State University
University Park
PA 16802, USA

The ORCID identification number(s) for the author(s) of this article can be found under https://doi.org/10.1002/apxr.202300003

DOI: 10.1002/apxr.202300003

a spontaneous polarization, P_s, many of the well-known piezoelectric and SHG crystals are also polar and often ferroelectric. Ferroelectricity induces an anharmonic ionic potential well and, in turn, an anharmonic electronic potential well. Therefore, conventional wisdom suggests that enhancing P_s would favor both piezoelectric and SHG tensors, though the magnitudes of the coefficients depend not just on the polarization, but also on the polarizability. This picture however is oversimplified. It is often possible to enhance the piezoelectricity by increasing the dielectric constant, and in many cases, this is coupled with a concomitant decrease in the spontaneous polarization, for example, in the wurtzite structures[9] as well as in numerous normal and relaxor ferroelectric perovskites.[11,12] Further, although molecules with a larger electric dipole,[13,14] and crystals with larger P_s,[15–19] often exhibit larger SHG responses, many commercial NLO crystals belong to the nonpolar point group $\bar{4}2m$.[20] It is shown in this work that instead of spontaneous polarization, the anharmonicities of the electronic and ionic potential wells determine the SHG and piezoelectric properties. For optical frequency conversion such as SHG, a broader frequency range of optical transparency is desired, which requires a larger electronic bandgap, E_g. However, a larger bandgap is known to reduce the SHG coefficients dramatically, limiting high conversion efficiency in the ultraviolet range.[20,21] Thus, increasing the piezoelectric tensor, d_{ijk}^{Piezo}, the SHG tensor, d_{ijk}^{SHG}, and the electronic bandgap, E_g, simultaneously in one material is a challenging balancing act.

Nonetheless, each of these phenomena, namely the d_{ijk}^{Piezo},[22–24] the d_{ijk}^{SHG},[25,26] the bandgap,[27–29] and in addition, the electro-optic tensor,[30] have been separately reported to be enhanced with Mg substitution in ZnO. This work revisits and confirms the first three of these experimental measurements in a single set of films, though the magnitudes of enhancement reported here significantly differ from the literature for d_{ijk}^{SHG}. Importantly, this work presents a unified theoretical framework for understanding these counterintuitive simultaneous enhancements. Finally, it reports, for the first time, precise ferroelectric domain engineering on the submicrometer scale.

ZnO is a well-known wide-bandgap semiconductor (E_g = 3.2 eV). Recently, $Zn_{1-x}Mg_xO$ was shown to have a giant switchable spontaneous polarization of ≈80 μC cm^{-2}.[31] In this work, it is demonstrated that the electronic bandgap, the SHG coefficient, and the piezoelectric coefficient are simultaneously enhanced by Mg substitution in $Zn_{1-x}Mg_xO$. Mg substitution induces a 30% increase in the bandgap and a simultaneous 50% enhancement in the SHG coefficients, contrary to the well-known inverse relationship between the two properties in the literature.[20,21] This is shown to be due to a 400% increase in the electronic anharmonicity that offsets the increasing bandgap and results in a net increase in the d^{SHG}. The ferroelectric polarization P_s decreases with higher Mg concentration (i.e., it anticorrelates to the increasing d^{SHG}), in contrast to the reported proportionality between P_s and SHG response.[15,16] Near 200% enhancement in the piezoelectric coefficient is observed in $Zn_{1-x}Mg_xO$ with increasing Mg addition, which is attributed to an increase in the low-frequency dielectric constant arising in part due to the softening of the wurtzite structure (reduced c/a ratio)[32,33] and a decrease in the anharmonicity of the ionic well. First-principles calculation and Landau theory provide a basis for understanding these trends. The piezoelectricity is enhanced by a small anharmonicity of the ionic potential well, while SHG is enhanced by a large anharmonicity of the electronic potential well. Here, harmonicity refers to the potential energy of the electron being proportional to the square of the displacement of the electron from its equilibrium position within the well, whereas in this work, anharmonicity will refer specifically to the potential energy term proportional to the cubic power of such electron displacements. (Higher order terms in such a Taylor expansion of the electron potential energy versus its displacement are also considered anharmonic but they will not be considered here). This work highlights the design paradigm of achieving both enhanced NLO properties and piezoelectric response by engineering anharmonicity differently in different frequency regimes. Because the polarization in $Zn_{1-x}Mg_xO$ is switchable, precise domain control can be achieved in these thin films down to 800 nm domain size, which enables optical quasi-phase-matched (QPM) SHG and domain-engineered electro-optic and piezoelectric devices with a materials growth process that is CMOS-compatible.[34,35]

2. Results and Discussion

$Zn_{1-x}Mg_xO$ films (x = 0, 16, 23, 28, 37 mol%) with a thickness of 150 nm were epitaxially grown at room temperature along the c-axis on (111)-Pt//(0001)-Al_2O_3 via RF magnetron sputtering from metal targets.[31] Over this range of x, $Zn_{1-x}Mg_xO$ adopts the wurtzite structure (**Figure 1**a) in PVD-grown thin films.[22,27,28] Mg substitutes on the Zn site due to their similar ionic radii and electronegativity, providing a local distortion of the bond lengths and angles.[31,36] Figure 1b shows the X-ray diffraction (XRD) and the film stack of (0001)-$Zn_{1-x}Mg_xO$//(111)-Pt//(0001)-Al_2O_3. $Zn_{1-x}Mg_xO$ maintains the wurtzite structure and high crystallinity without forming a secondary rocksalt phase.[22,31,36] The (0002)-$Zn_{1-x}Mg_xO$ peak shifts gradually toward a higher 2θ in XRD with increasing Mg concentration. This indicates a systematic contraction in the c-lattice constant by Mg substitution, which agrees well with the previous studies.[22,27,31] The films are epitaxial to the underlying Pt electrode and have an out-of-plane full-width-half-maximum value in the omega x-ray circle between 1.5° and 2.0° at the lowest and highest Mg concentrations, respectively. An expansion along the a axis and an overall reduction in the c/a ratio have also been reported for comparable films.[22,27,31] Scanning electron microscopy (SEM) was performed to evaluate the surface microstructure, while surface roughness was measured by atomic force microscopy (AFM). Results reveal uniform faceted surface grains with an average diameter of ≈100 nm and smooth surface (RMS roughness = 1.3 nm) (Figure S1, Supporting Information). These observations illustrate high-quality films for further optical and electromechanical studies. Figure 1c exhibits the hysteresis loop for $Zn_{0.63}Mg_{0.37}O$, demonstrating that the ferroelectricity emerges beyond the critical concentration (≈34%).[31] Although the polarization in ZnO is not switchable, alloying with Mg has been proven to be an effective way to access the ferroelectricity without further external stimuli. The coercive field is found to be around 3 MV cm^{-1}, similar to that reported in previous studies.[31]

The bandgap measurements are discussed first, then the SHG measurements, followed by the piezoelectric measurements. The complex linear optical refractive indices ($\tilde{n} = n + ik$) (Figure 1d)

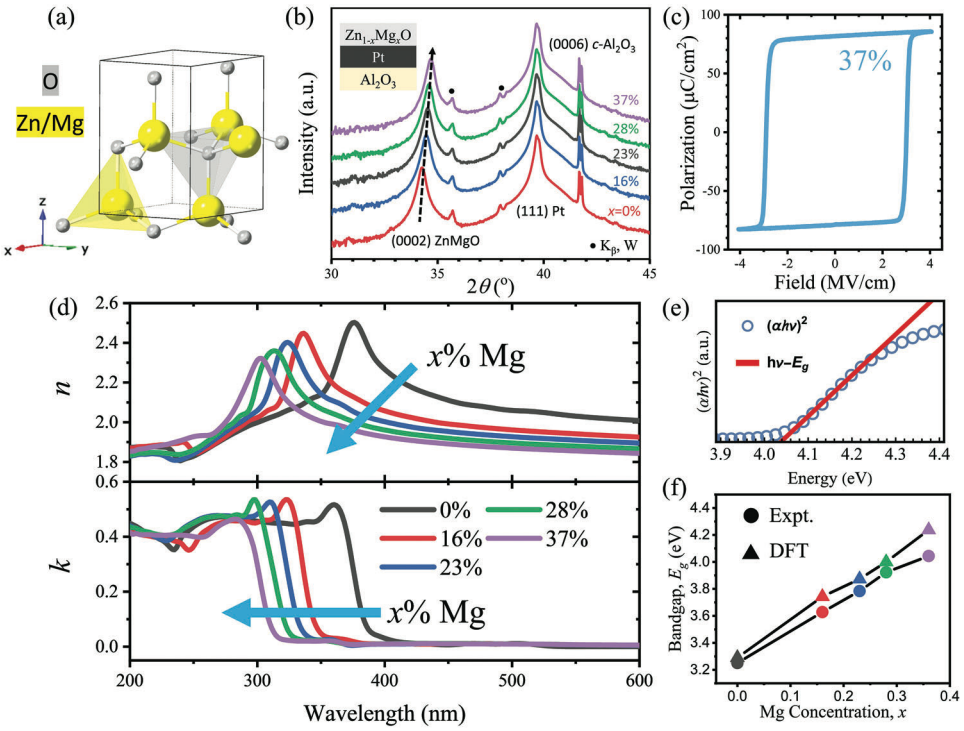

Figure 1. Crystal structure, X-ray diffraction (XRD), and linear optical properties of $Zn_{1-x}Mg_xO$. a) Wurtzite structure of $Zn_{1-x}Mg_xO$. b) X-ray diffraction for a series Mg concentration ($x = 0$, 0.16, 0.23, 0.28, and 0.37). The dashed line highlights the $Zn_{1-x}Mg_xO$ (0002) peak as a function of Mg concentration. Asterisks indicate K_β, W peaks. c) P–E hysteresis loop for $Zn_{0.63}Mg_{0.37}O$. d) Complex refractive indices $\tilde{n} = n + ik$ of $Zn_{1-x}Mg_xO$ from 200 to 600 nm. e) Tauc fitting of $Zn_{0.63}$ $Mg_{0.37}O$. The dotted and solid lines represent experimental results and fit, respectively. f) Bandgaps of $Zn_{1-x}Mg_xO$ as a function of Mg concentration. The circle represents experimental results, and the triangle stands for DFT.

were studied using spectroscopic ellipsometry from 1800 to 200 nm (equivalent to 0.69 to 6.2 eV). Mg substitution reduces the refractive indices and pushes the band edge toward higher energy. Since the experimental bandgaps of ZnO and MgO are reported to be 3.2 and 7.8 eV,[37,38] respectively, Mg addition is expected to increase the bandgap. The refractive indices below the band edges were fitted using the birefringent Cauchy dispersion relation due to the uniaxial structure of $Zn_{1-x}Mg_xO$, and the Cauchy parameters are summarized in Table S1 (Supporting Information). Using the Tauc method[39,40] and the measured n and k of $Zn_{1-x}Mg_xO$, a direct band transition was confirmed throughout the $Zn_{1-x}Mg_xO$ series from $x = 0$ to 0.37. As expected, adding Mg reduces the refractive indices and pushes the band edge toward higher energy. The Tauc fitting for $x = 0.37$ is shown in Figure 1e, which results in the largest bandgap in the series. The extracted bandgaps as a function of Mg concentration from the experiment (Figure 1f) show a linear dependence on the Mg concentration, which agrees well with previous studies and is in agreement with the DFT predictions.[28,29]

SHG is a NLO process that converts two photons at ω frequency to one photon at 2ω frequency.[41] SHG has been widely applied in coherent lasing sources, structural characterization, and biological imaging. **Figure 2**a exhibits the experimental geometry of the SHG measurement. The incident polarization (E^ω) is rotated by a half-wave plate (azimuthal angle φ), and both p- and s- polarized SHG intensities ($I_p^{2\omega}$ and $I_s^{2\omega}$) were collected as a function of incident polarization φ. The measured films are a stack of (0001)-$Zn_{1-x}Mg_xO$//(111)-Pt//(0001)-Al_2O_3.

Due to the strong reflection and absorption of the Pt layer at ω and 2ω frequencies, multireflection and absorption of both the fundamental ω and second harmonic 2ω waves (Figure 2b) need to be considered to correctly model and extract second-order nonlinear susceptibilities. It is noted that typical NLO analysis involves numerous assumptions, such as the slowly varying amplitude approximation,[21] weak reflection of the nonlinear source wave,[42,43] and Kleinman's symmetry.[44–46] Excluding multiple reflections in the optical analysis would lead to a failure of available SHG models.[42,43] Kleinman's symmetry forces $d_{31}^{SHG} = d_{15}^{SHG}$ in Voigt notation in the $Zn_{1-x}Mg_xO$ system which could be problematic and therefore is not assumed *a priori* in the analysis presented in this current study.[41,47] Failure to take all necessary effects into account can result in one to two orders of magnitude error in the estimation of the SHG coefficients as compared with bulk single crystals. An advanced modeling tool named ♯SHAARP was employed, which fully accounts for multiple reflections, interference, and the complete anisotropic SHG tensor.[47]

The polarized second harmonic intensities (dots) and fitting (solid lines) are shown in Figure 2c, where blue and red represent p- and s- polarized intensity, respectively. The power-dependent

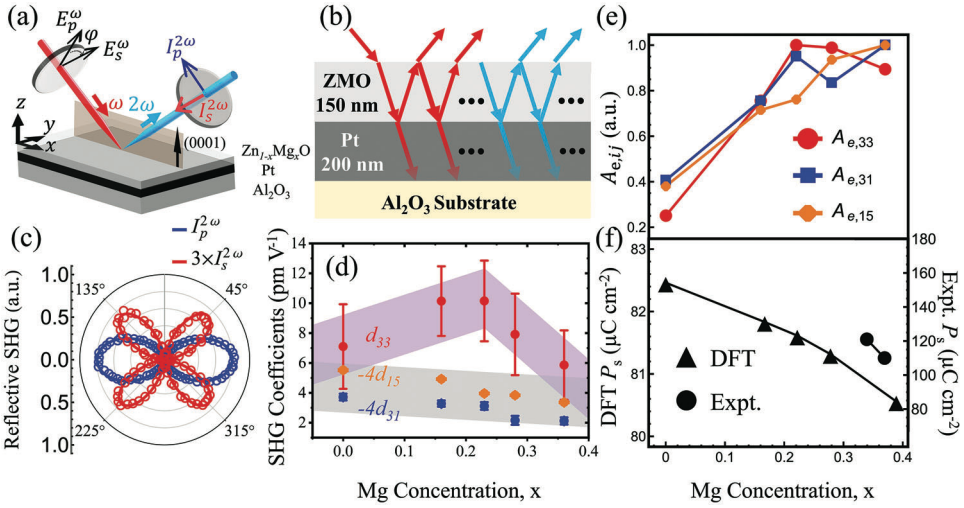

Figure 2. Nonlinear optical (NLO) properties of $Zn_{1-x}Mg_xO$. a) Experimental geometry of second harmonic generation (SHG). Red and blue rays are the fundamental wavelength and SHG wavelength, respectively. b) Multireflection model for SHG analysis. Red and blue waves correspond to the fundamental and SHG waves. ZMO refers to $Zn_{1-x}Mg_xO$. c) SHG polarimetry of $Zn_{1-x}Mg_xO$. Blue and red correspond to *p*- and *s*- polarized second harmonic intensity. The dotted and solid lines represent the experimental results and fit separately. d) Absolute SHG coefficients of $Zn_{1-x}Mg_xO$ films. d_{33}^{SHG}, d_{31}^{SHG}, and d_{15}^{SHG} are colored in red, blue, and orange. The background trendlines are a guide to the eye. e) Relative anisotropic anharmonicity $A_{e,ij}$ change for three SHG coefficients using the same color scale as (d). f) Spontaneous polarization from DFT and remanent polarization from the experiment. Triangles and circles represent DFT and experimental results.

SHG response shows a quadratic dependence between pump power and SHG intensity, $I^{2\omega} \propto (I^{\omega})^2$, confirming intrinsic SHG response from the $Zn_{1-x}Mg_xO$ films (Figure S2, Supporting Information). The absolute second harmonic susceptibilities of $Zn_{1-x}Mg_xO$ are extracted by referencing against a well-studied $LiNbO_3$ single crystal and are summarized in Figure 2d, Table S2, and Equations S7–S26 (Supporting Information). A 0.5 mm thick ZnO single crystal was also studied to verify and benchmark the analysis. The absolute SHG susceptibility d_{33}^{SHG} of the ZnO single crystal is found to be 7.30 pm V^{-1}, which agrees well with reported values in the literature.[45,46,48] This indicates a robust and reliable methodology using #SHAARP[47] for the characterization of NLO response (Figure S3, Supporting Information). Figure 2d summarizes the absolute SHG susceptibilities of $Zn_{1-x}Mg_xO$ as a function of Mg concentration, where E_g increases monotonically with the Mg concentration. Interestingly, a nearly 50% enhancement of d_{33}^{SHG} is found in $x = 0.16$ and 0.23 as compared to pure ZnO films and single crystals. This enhancement is significantly less than the enhancement of 420% reported in the literature;[25] Such large previously reported SHG coefficients (approaching ≈50 pm V^{-1}) for wide bandgap semiconductors such as ZnO are unusual. A slightly different wavelength or the details of the film growth are likely minor contributors to this discrepancy since the pure ZnO film in our current study exhibits SHG coefficients similar to the bulk crystal. The most likely source of the discrepancy we surmise is the modeling of the SHG response in the thin film. For example, if we assume Kleiman's symmetry in our case, it can erroneously result in ≈50 pm V^{-1} of d_{33}^{SHG} for both $x = 0.28$ and 0.37, suggesting a possible reason for such discrepancy (Figure S6, Supporting Information). Given our confidence in taking care of all the relevant details in modeling using the proven #SHAARP code and benchmark analysis using both films and the single crystal, the prior reported enhancement needs to be revisited.[25] Further Mg substitution beyond 23% Mg tends to suppress d_{33}^{SHG} before reaching the maximum solubility. On the other hand, both the raw d_{31}^{SHG} and d_{15}^{SHG} exhibit a monotonic reduction with increasing Mg concentration; nonetheless as shown below, the electronic anharmonicity increases with the Mg concentration for these coefficients as well.

In the classical nonlinear spring model, the energy dispersion of the SHG nonlinear susceptibility is given by, $d_{ij}^{SHG} \propto A_{e,ij}(E_g^2 - 4E_{photon}^2)^{-1}(E_g^2 - E_{photon}^2)^{-2}$, where d^{SHG}, $A_{e,ij}$, E_g, and E_{photon} are the SHG susceptibility, anharmonicity of the nonlinear spring, bandgap, and probing photon energy.[21,41] In particular, $A_{e,ij}$ is the strength of the lowest power anharmonic term in the energy profile for a bound electron oscillating with respect to its nuclei. The anharmonicity, $A_{e,ij}$, describes the origin of SHG response and captures the underlying physics for designing highly efficient NLO crystals, including planar triangle anion groups, second-order Jahn-Teller effects, and lone pair electrons.[15,49] Based on this dependence, d^{SHG} tends to be suppressed by the larger bandgap at higher Mg concentrations.[50] However, nearly 50% enhancement of d_{33}^{SHG} up to 23% Mg is observed along with the bandgap widening. By correcting the raw d_{ij}^{SHG} data in Figure 2d for the dispersion term, $(E_g^2 - 4E_{photon}^2)^{-1}(E_g^2 - E_{photon}^2)^{-2}$, one can obtain a quantity proportional to the anharmonicity of the electronic well, $A_{e,ij}$ as shown in Figure 2e. The increase of $A_{e,ij}$ for all three susceptibilities suggests that Mg substitution promotes the anharmonicity of the electronic potential well along both the ordinary and the extraordinary polarization directions. In particular, a roughly 400% enhancement of the $A_{e,33}$ is observed, indicating a more significant influence on the electronic potential well along the polar direction. Simultaneously, the spontaneous polarization, P_s decreases as a function of Mg concentration experimentally (Figure 2f);[31] DFT calculations

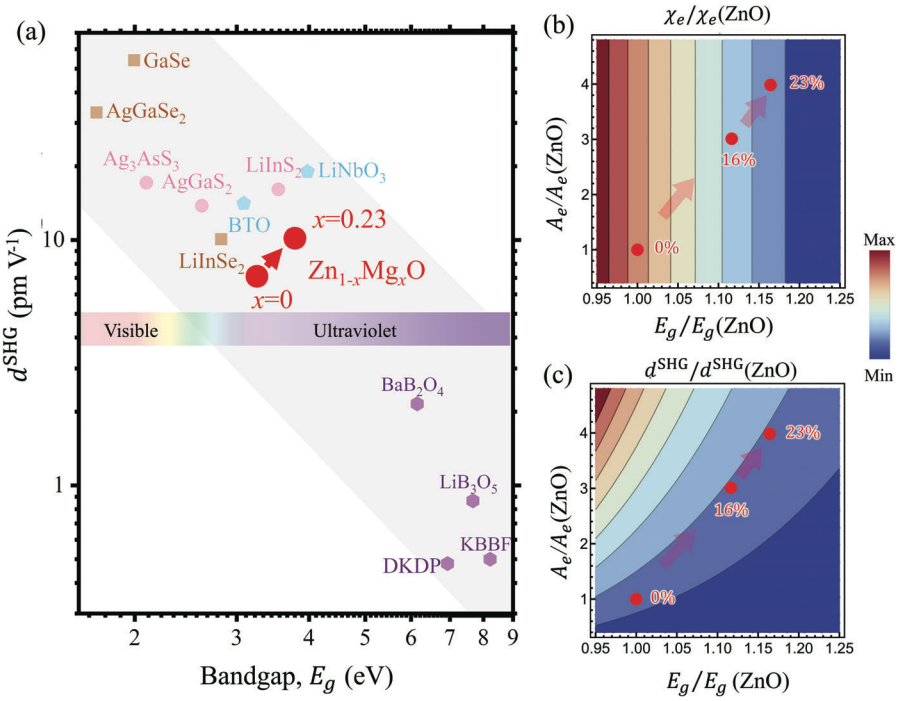

Figure 3. Competing effects among bandgap (E_g), anharmonicity (A_e), and second harmonic generation (SHG) susceptibility (d^{SHG}). a) Summary of SHG coefficients and bandgaps among various nonlinear optical (NLO) materials and $Zn_{1-x}Mg_xO$. The labels BTO, DKDP, and KBBF stand for $BaTiO_3$, KD_2PO_4, and $KBe_2BO_3F_2$, respectively. The gray region is a guide to the eyes of the relationship between d^{SHG} and E_g. b,c) Contour plot of (b) electronic dielectric susceptibility χ_e and (c) SHG coefficients d^{SHG} as a function of normalized E_g and $A_{e,33}$ relative to the ZnO using Equations (1) and (2). N_e, m, $\hbar$, e and ϵ_0 are set to unit values. The red arrows show the trajectory of the change from $x = 0$ to 23% in $Zn_{1-x}Mg_xO$.

attribute this trend mainly to the reduced Born effective charge of Zn and Mg, from 2.17 in ZnO to an average of 2.03 in $Zn_{0.61}Mg_{0.39}O$ along the c direction. Thus, the substantial enhancement of d_{33}^{SHG} and $A_{e,33}$ in this material system are both found to be inversely correlated to the change in the spontaneous polarization, contrary to conventional expectations,[16,51,52] suggesting that it is the electronic anharmonicity rather that the spontaneous polarization that determines the SHG coefficients.

Figure 3a summarizes the d^{SHG} and E_g among state-of-art NLO materials.[20] With increasing bandgaps, the magnitudes of NLO susceptibilities reduce dramatically. Remarkably, $Zn_{1-x}Mg_xO$ with x from 0% to 23% clearly demonstrates a substantial enhancement of both d^{SHG} and E_g, contrary to the general trend (highlighted in gray) observed across a broad range of material families.

To develop some intuitive understanding of the mechanism that supports this contrary trend, let us consider a classical anharmonic electronic potential well given by $U_e = \frac{mE_g^2}{2\hbar^2}x^2 + \frac{mA_e}{3}x^3 + \cdots$, where U_e, E_g, A_e, m, $\hbar$, and x are, respectively, the electronic potential energy, electronic bandgap, anharmonicity of the oscillator, effective mass, reduced Planck constant, and the electron position.[21,41] Using the classical theory of anharmonicity, one can derive expressions for the dielectric susceptibility (χ_e) and d^{SHG} as a function of E_g and A_e for the nonresonant SHG process as shown in Equations (1) and (2):[21,41]

$$\chi_e = \frac{N_e e^2 \hbar^2}{\epsilon_0 m E_g^2 - \epsilon_0 m E_{photon}^2} \quad (1)$$

$$d^{SHG} = \frac{N_e A_e e^3 \hbar^6}{m^2 \left(E_g^2 - 4E_{photon}^2\right)\left(E_g^2 - E_{photon}^2\right)^2} \quad (2)$$

where ϵ_0 is the vacuum permittivity, N_e is the number of dipoles per unit volume, e is the electron charge, and E_{photon} is the experimental pumping energy at 0.8 eV. Experimental observation has confirmed a ≈16% increase in the E_g and 400% enhancement in the $A_{e,33}$ from $x = 0\%$ to 23%. Figure 3b,c illustrates the relative changes of χ_e and d^{SHG} as compared with pure ZnO following Equations (1) and (2). With increasing E_g, the χ_e decreases due to the reduction of the electronic polarizability, as seen in Figure 3b. Normally, an increasing E_g tends to suppress the magnitude of d^{SHG} for a given A_e as seen in Figure 3a. However, in $Zn_{1-x}Mg_xO$, a substantial enhancement of $A_{e,33}$ offsets the effect of increasing E_g and decreasing χ_e to yield a net increase in d^{SHG}, as indicated in Figure 3c. Increasing Mg concentration tends to reduce the Zn-O bond length, as confirmed by the lattice parameters.[31] Since the decrease in the bond length will promote the Coulomb repulsion between Zn(Mg) and O, it is postulated that the distorted O-$2p_z$ and the Zn $3d$ and Mg $2p$ orbitals are likely the driving force for the enhanced nonlinearity in the $Zn_{1-x}Mg_xO$ system. These orbitals dominate the density of states near the band edge, and thus are the major source for the non-resonant SHG response.[53,54]

Next, the enhancement in the piezoelectric coefficients is discussed. **Figure 4** summarizes the piezoelectric response and writing of periodically poled ferroelectric domains in $Zn_{1-x}Mg_xO$ using a combination of interferometric displacement sensing

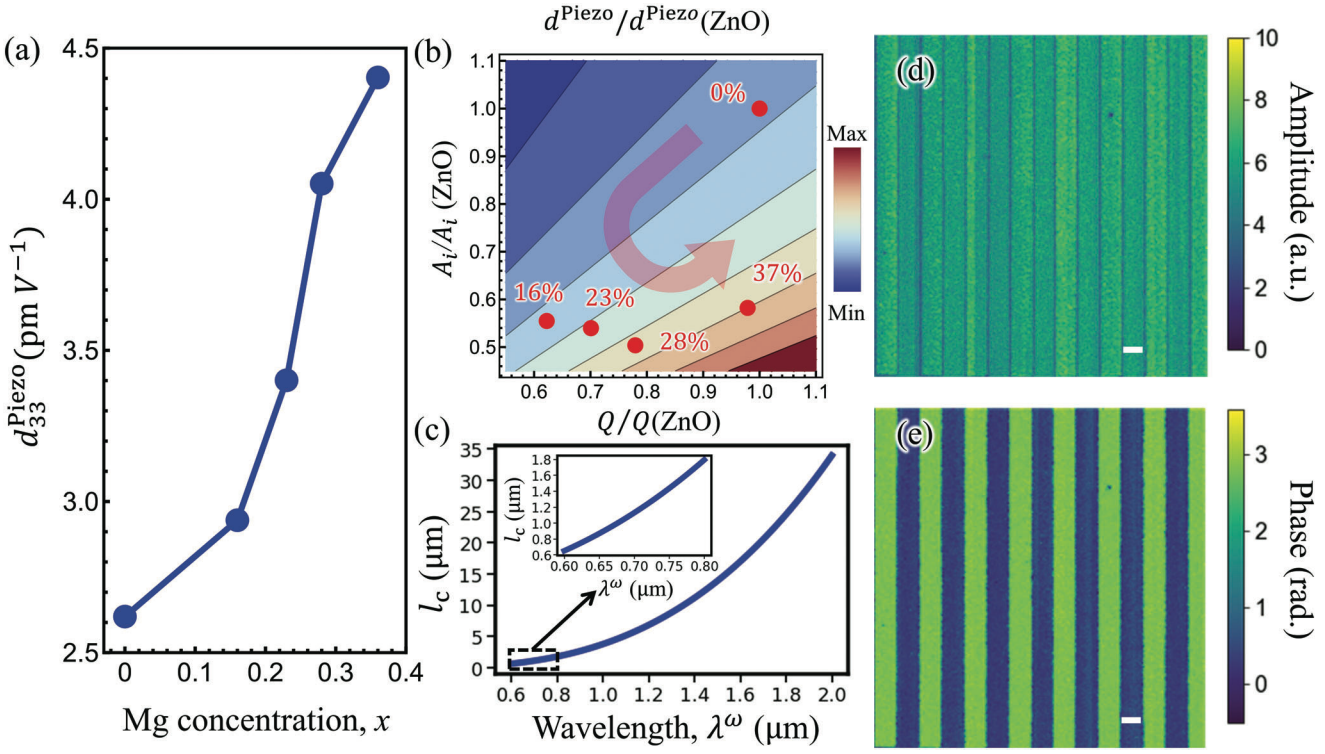

Figure 4. Piezoelectric force microscopy (PFM) results and quasi-phase-matched (QPM) of $Zn_{1-x}Mg_xO$. a) d_{33}^{Piezo} acquired from interferometric displacement sensing (IDS) PFM on $Zn_{1-x}Mg_xO$ series. b) Contour plot of d^{Piezo} as a function of Q and A_i relative to the ZnO. ϵ_0 is set to the unit value. The red arrow indicates the changes from $x = 0$ to 0.37 in $Zn_{1-x}Mg_xO$. c) Coherence length (l_c) as a function of the fundamental wavelength λ^{ω} of $Zn_{0.63}Mg_{0.37}O$ for QPM second harmonic generation (SHG) devices. The inset shows a zoomed-in wavelength range between 0.6 – 0.8 μm. d,e) Band excitation piezoelectric force microscopy (BE-PFM) mapping of periodically poled $Zn_{0.63}Mg_{0.37}O$ with a scan size of 12.8 × 12.8 μm poled at ±50V. d) Amplitude, and e) phase. The scale bars in panels (d) and (e) are 0.8 μm.

(IDS) and band excitation piezoelectric force microscopy (BE-PFM). The as-grown films exhibit uniform PFM phase across the scanned area, indicating that the films were single domain as-deposited with a spontaneous polarization pointing down in their initial state (Figure S4, Supporting Information). The piezoelectric coefficient (d_{33}^{Piezo}), extracted from the out-of-plane electromechanical displacements measured via IDS as a function of applied AC voltage, are shown in Figure 4a across the $Zn_{1-x}Mg_xO$ concentration series. Here, nearly a twofold increase in d_{33}^{Piezo} is observed between Mg concentrations of $x = 0.0$ and 0.37, consistent with the enhancement observed in prior literature.[22–24] The discrepancy in the magnitude of d_{33}^{Piezo} between our work and other studies is likely due to the clamping effect from the substrate in our thinner epitaxial films.

To understand this enhancement in d_{33}^{Piezo}, a Landau–Ginzburg–Devonshire (LGD) theory prediction of the piezoelectric coefficient is utilized.[55–57] Starting from the free energy of a system, one can derive the piezoelectric coefficients, given as $d^{Piezo} = 2QP_s\ \chi_i = \frac{Q}{\epsilon_0 A_i}$, where χ_i is the linear ionic susceptibility tensor, Q is the electrostrictive tensor and A_i is the anharmonicity tensor of the ionic potential well of the Zn or Mg ions in the oxygen tetrahedral cage (Equations S1–S6 and Figure S5, Supporting Information). According to the Gibbs free energy of ferroelectrics, A_i represents the magnitude of the cubic term in the Taylor expansion of the ionic potential energy near its equilibrium position at $P = P_s$. Based on the changes in d^{Piezo}, P_s and χ_i, the ionic anharmonicity and electrostrictive coefficient can be quantitatively analyzed.[31] Figure 4b highlights the changes in Q, A_i and the corresponding d^{Piezo} among $Zn_{1-x}Mg_xO$ concentrations. Between $x = 0\%$ and 37%, Q varies only slightly (less than 5%), indicating that the electrostrictive response is not the major factor enhancing the piezoelectric response. On the other hand, P_s from DFT exhibits a ≈2% reduction (Figure 2f) and the reported ionic dielectric susceptibility, χ_i, exhibits a ≈75% enhancement,[31] resulting in ≈40% reduction in the anharmonicity of the ionic potential well between $x = 0$ and 0.37. ($A_i = \frac{1}{2\epsilon_0 P_S \chi_i}$ as derived in Section S7, Supporting Information) The reduced ionic anharmonicity combined with a slight change in the electrostriction produces a nearly 200% enhancement in the piezoelectric coefficient. The smaller anharmonicity A_i of the ionic potential well has a similar effect in $Zn_{1-x}Mg_xO$ as the double well potential flattening on approaching a phase boundary in perovskite piezoelectrics (Figure S5, Supporting Information).[55,56,57,58,59] Applying LGD theory in $Zn_{1-x}Mg_xO$ also predicts the lowering of the energy barrier of ferroelectric switching with increasing Mg concentration (Figure S5c, Supporting Information). This further provides insight into the polarization switching mechanism from polar ZnO toward ferroelectric $Zn_{1-x}Mg_xO$. The softening of the wurtzite structure (smaller c/a ratio) and flattened double

well potential lower the energy barrier of the polarization reversal, facilitating cation motion through the oxygen at the base of the tetrahedron to reverse the spontaneous polarization. This theoretical framework agrees well with experimental observations of enhanced dielectric constant,[31] increased piezoelectric response, reduction in spontaneous polarization, and switchable ferroelectric polarization with increasing Mg concentration in $Zn_{1-x}Mg_xO$, as demonstrated in this study.

To highlight the potential technological interest in this material, PFM was utilized to demonstrate fine control over domain patterning in ferroelectric $Zn_{1-x}Mg_xO$. Domain reversal with electric fields is far simpler and preferred as compared with domain reversal during synthesis using engineered surface termination in AlN,[60,61] and polarity control in ZnO.[62] Coherence length (l_c) is the size of the domain in a domain grating of period $2l_c$ required for quasi-phase-matched SHG, defined as $l_c = \lambda^{\omega}/4(n^{2\omega} - n^{\omega})$, where λ and n are wavelength and refractive index, and superscript ω represents the corresponding frequency.[63] The calculated l_c as a function of fundamental wavelength λ^{ω} in $Zn_{0.63}Mg_{0.37}O$ is illustrated in Figure 4c. The l_c is found to be 800 nm when a wavelength of $\lambda^{\omega} = 650$ nm is halved to $\lambda^{2\omega} = 325$ nm. The theoretical limit of l_c is found to be ≈650 nm when $\lambda^{2\omega}$ approaches the band edge, the limit of the useful range for nonlinear optics. As proof of the feasibility of QPM in $Zn_{1-x}Mg_xO$, a periodic poled pattern with a domain width of 800 nm is demonstrated in $Zn_{0.63}Mg_{0.37}O$. The BE-PFM amplitude (Figure 4d) and phase (Figure 4e) show a clear domain contrast with opposite polarization, demonstrating the realization of precise and controllable QPM for any targeted wavelength below the bandgap.

3. Conclusion

In summary, $Zn_{1-x}Mg_xO$ brings exceptional optical, electrical, and electromechanical responses to life in a single multifunctional platform. The simultaneous increase in both the second-order NLO susceptibility and the optical bandgap in $Zn_{1-x}Mg_xO$ suggests that increasing the anharmonicity of the electron potential well can offset a bandgap increase for designing NLO materials in the ultraviolet spectral region. On the low-frequency end, adding Mg reduces the anharmonicity of the ionic potential well, leading to an enhancement of the piezoelectric response. This study thus demonstrates that the anharmonicity can be independently engineered in the optical and low-frequency regimes through chemical pressure. This may be key to optimizing exceptional piezoelectric and NLO response in one material. Moreover, precisely controlled periodic ferroelectric domain patterns for optical QPM were demonstrated in $Zn_{1-x}Mg_xO$, which opens new possibilities for NLO optical waveguides for efficient NLO conversion and all-optical switching schemes deeper into the ultraviolet range. The presence of ferroelectricity with large polarization, high ionic dielectric susceptibility, improved piezoelectric response, large tunable bandgap, and significantly enhanced SHG response make $Zn_{1-x}Mg_xO$ a promising candidate for applications such as microelectromechanical systems, integrated optics, nonlinear photonics, and strain-tunable photonics.

4. Experimental Section

Growth of $Zn_{1-x}Mg_xO$ Films, XRD, SEM, EDS, AFM: $Zn_{1-x}Mg_xO$ thin films were grown via a radio frequency (RF) magnetron co-sputtering technique using metallic Zn and Mg targets. A 2-inch (0001)-Al_2O_3 wafer was rinsed successively in isopropanol, methanol and acetone for 1 min, followed by an ultraviolet ozone treatment for 10 min. The wafer was placed in a sputtering chamber until the base pressure was reduced to 1×10^{-7} Torr at 300 °C. Deposition of a 200 nm thick (111)-Pt layer on (0001)-Al_2O_3 was performed at 10 mTorr in Ar atmosphere. $Zn_{1-x}Mg_xO$ thin films were then sputtered on the (111)Pt//(0001)-Al_2O_3 substrate at room temperature. During depositions, a gas flow of Ar and O was fixed to 16 and 4 sccm, respectively, and a total pressure was kept to 4 mTorr. The Mg content was controlled by changing the Mg target power between 0 to 48 W, while the Zn target power was fixed at 23 W. The chemical composition and surface morphology were confirmed by energy dispersive spectroscopy (EDS) and SEM in Zeiss Sigma. Crystal structure was investigated via XRD using Cu–Kα1 (1.5406 Å) in a Panalytical Empyrean, and the surface roughness was measured using AFM in Asylum MFP3D.

Optical Spectroscopic Ellipsometry: Optical spectroscopic ellipsometry was conducted using Woollam M-2000 and Woollam M-2000F spectroscopic ellipsometers. Woollam M-2000F has a fixed incident angle of around 60°, and three incident angles (55°, 65°, and 75°) were collected using Woollam M-2000. The two results are cross confirmed and combined to reveal the complex refractive indices from 200 to 1800 nm using the same model.

Tauc Method for Optical Bandgap: The Tauc equation is expressed as $(\alpha h\nu)^{1/n} = A(h\nu - E_g)$, where α, h, ν, A, and E_g are the absorption coefficient, Planck's constant, photon frequency, proportionality constant, and bandgap.[40] n is the measure of direct or indirect transition and n is set to 0.5 for the best fitting condition in this study.

SHG Measurement: SHG has been widely used to confirm noncentrosymmetric structures, ferroelectric response, and wavelength conversion efficiency. The polarization-resolved SHG measurements were carried out at room temperature in 45-degree reflection mode on samples. The SHG measurement is an all-optical technique where two photons of frequency ω with fields E_j and E_k and polarization directions j and k, respectively, interact with a material with a non-zero d_{ijk} tensor and generate a polarization $P_i^{2\omega}$ of frequency 2ω in the i direction. The SHG intensity, $I^{2\omega}$, was detected with a Hamamatsu photomultiplier tube. A Ti-sapphire laser (Spectra-Physics) with an output of 800 nm, 80 fs pulses at 2 kHz frequency was used. The fundamental light with a central wavelength at 1550 nm was generated through an optical parametric amplifier after the Coherent Libra Amplified Ti: Sapphire femtosecond laser system (85 fs, 2 kHz). Here, (x, y, z) is the lab coordinate system where experiments are performed. The plane of incidence is defined in the x--z plane, and z corresponds to the surface normal. The surface normal of $Zn_{1-x}Mg_xO$ is the (0001) plane.

Electronic-Structure Calculations: First-principles calculations were performed using norm-conserving pseudopotentials within the Perdew–Burke–Ernzerhof (PBE) approximation to the exchange-correlation energy.[64–72] Supercell structures were generated using the Atomic Simulation Environment (ASE) module.[73] To consider atomic fraction of $x = 0$–40%, a supercell size of $3 \times 3 \times 2$ was considered with minimal Mg clustering. The ***k***-point spacing in the first Brillouin zone was set to 0.05 $Å^{-1}$, and the kinetic energy cutoff for the electronic wavefunctions was set to 80 Ry with a charge density cutoff of 320 Ry. The lattice parameters and c/a ratios of the unit cell of ZnO and the supercell structures of $Zn_{1-x}Mg_xO$ were calculated using geometry optimization. The total energy and force thresholds were set to 10^{-5} Ry and 10^{-4} Ry $bohr^{-1}$, respectively. Band gaps were calculated within the DFT+U approximation at fixed (PBE) geometry.[74] Unlike the empirical approach that consists of adjusting the Hubbard U parameters to match experimental bandgaps, the Hubbard U parameters were calculated using an entirely nonempirical method via density functional perturbation theory (DFPT).[75–77] A detailed description of this nonempirical DFT+U framework is provided in the Supporting information. Following ref. [76] the Hubbard U parameters were applied to O-2p orbitals (cf. Tables S3 and S4, Supporting

Information). Using this approach, the spontaneous polarization was calculated via the Berry phase method.[78,79]

IDS-PFM, BEPFM Measurement, Periodic Poling: IDS PFM measurements were taken using an Oxford Instruments Cypher atomic force microscope equipped with a Polytec OFV-5000 Modular Vibrometer routed to the tip for measuring tip displacements, i.e., the piezoelectric coefficient (d_{33}^{Piezo}). AC voltages ranging from 2 to 10 V at 40 kHz were used for a linear extraction of d_{33}^{Piezo}, i.e. the slope of IDS-PFM amplitude versus applied AC voltage. The BE PFM measurements were acquired using an Oxford Instruments Cypher atomic force microscope with an imaging AC voltage of 2 V, and periodic poling voltage of ±50 V. Details describing BE functionality can be found elsewhere.[80] For all atomic force microscopy measurements, Budget Sensor Electri Muli75-G Cr/Pt coated probes were used.

Remanent Polarization Measurement: Remanent polarization values for Pt/ZMO/Pt capacitors were extracted from bipolar polarization–electric field (*P*–*E*) hysteresis loops driven at ≥4 MV cm^{-1} with a 100 Hz triangle wave at room temperature. A precision Multiferroic II tester (Radiant Technologies) was used to measure the *P*–*E* loops and to extract the remanent polarization values. Each reported value was averaged over 10 measurements on five capacitors.

Supporting Information

Supporting Information is available from the Wiley Online Library or from the author.

Acknowledgements

R.Z., G.R., S.B., L.C.J., I.D., S.T-M., J-P.M., and V. G. were primarily supported as part of the center for 3D Ferroelectric Microelectronics (3DFeM), an Energy Frontier Research Center funded by the U.S. Department of Energy (DOE), Office of Science, Basic Energy Sciences under Award Number DE-SC0021118, for the new materials development. R.Z. also received support from the NSF MRSEC Center for Nanoscale Science, DMR-2011839, for optical characterizations. The Piezoresponse Force Microscopy research was supported by the Center for Nanophase Materials Sciences (CNMS), which is a US Department of Energy, Office of Science User Facility at Oak Ridge National Laboratory. B.W. and L.-Q.C. were supported by the National Science Foundation under the grant number DMR-2133373. Computational resources were provided through the Pennsylvania State University's Roar supercomputers within the Institute for Computational and Data Sciences. J.H. acknowledges support from NSF DMR-2210933.

Conflict of Interest

The authors declare no conflict of interest.

Data Availability Statement

The data that support the findings of this study are available from the corresponding author upon reasonable request.

Keywords

bandgaps, ferroelectricity, piezoelectricity, second harmonic generation, thin films, ZnO

Received: January 13, 2023
Revised: April 22, 2023
Published online:

[1] N. L. Bishop, V. Kradinov, P. B. Reid, T. N. Jackson, C. T. DeRoo, S. Trolier-McKinstry, *J. Astron. Telesc. Instrum. Syst.* **2022**, *8*, 029004.
[2] R. H. T. Wilke, R. L. Johnson-Wilke, V. Cotroneo, S. McMuldroch, P. B. Reid, D. A. Schwartz, S. Trolier-McKinstry, *IEEE Trans. Ultrason. Ferroelectr. Freq. Control* **2014**, *61*, 1386.
[3] L.-H. Peng, C.-W. Chuang, L.-H. Lou, *Appl. Phys. Lett.* **1999**, *74*, 795.
[4] D. F. Nelson, E. H. Turner, *J. Appl. Phys.* **1968**, *39*, 3337.
[5] S. Kim, V. Gopalan, *Appl. Phys. Lett.* **2001**, *78*, 3015.
[6] N. Malkova, V. Gopalan, *Phys. Rev. B* **2003**, *68*, 245115.
[7] N. Malkova, S. Kim, V. Gopalan, *Appl. Phys. Lett.* **2003**, *83*, 1509.
[8] D. Scrymgeour, N. Malkova, S. Kim, V. Gopalan, *Appl. Phys. Lett.* **2003**, *82*, 3176.
[9] S. Trolier-McKinstry, S. Zhang, A. J. Bell, X. Tan, *Annu. Rev. Mater. Res.* **2018**, *48*, 191.
[10] X. Liu, P. Tan, X. Ma, D. Wang, X. Jin, Y. Liu, B. Xu, L. Qiao, C. Qiu, B. Wang, W. Zhao, C. Wei, K. Song, H. Guo, X. Li, S. Li, X. Wei, L.-Q. Chen, Z. Xu, F. Li, H. Tian, S. Zhang, *Science* **2022**, *376*, 371.
[11] F. Li, M. J. Cabral, B. Xu, Z. Cheng, E. C. Dickey, J. M. LeBeau, J. Wang, J. Luo, S. Taylor, W. Hackenberger, L. Bellaiche, Z. Xu, L.-Q. Chen, T. R. Shrout, S. Zhang, *Science* **2019**, *364*, 264.
[12] F. Li, D. Lin, Z. Chen, Z. Cheng, J. Wang, C. Li, Z. Xu, Q. Huang, X. Liao, L.-Q. Chen, T. R. Shrout, S. Zhang, *Nat. Mater.* **2018**, *17*, 349.
[13] T. Handa, R. Hashimoto, G. Yumoto, T. Nakamura, A. Wakamiya, Y. Kanemitsu, *Sci. Adv.* **2022**, *8*, eabo1621.
[14] T. W. Kasel, Z. Deng, A. M. Mroz, C. H. Hendon, K. T. Butler, P. Canepa, *Chem. Sci.* **2019**, *10*, 8187.
[15] H. Wu, H. Yu, Z. Yang, X. Hou, X. Su, S. Pan, K. R. Poeppelmeier, J. M. Rondinelli, *J. Am. Chem. Soc.* **2013**, *135*, 4215.
[16] D. K. T. Chu, H. Hsiung, *Appl. Phys. Lett.* **1992**, *61*, 1766.
[17] C. Liu, K. Gao, Z. Cui, L. Gao, D.-W. Fu, H.-L. Cai, X. S. Wu, *J. Phys. Chem. Lett.* **2016**, *7*, 1756.
[18] R. C. Miller, *Phys. Rev.* **1964**, *134*, A1313.
[19] B. Sahraoui, R. Czaplicki, A. Klöpperpieper, A. S. Andrushchak, A. V. Kityk, *J. Appl. Phys.* **2010**, *107*, 113526.
[20] D. N. Nikogosyan, *Nonlinear Optical Crystals: A Complete Survey*, Springer Science & Business Media, Berlin **2006**.
[21] R. W. Boyd, D. Prato, *Nonlinear Optics*, Academic Press, Amsterdam, Boston **2008**.
[22] X. Kang, S. Shetty, L. Garten, J. F. Ihlefeld, S. Trolier-McKinstry, J.-P. Maria, *Appl. Phys. Lett.* **2017**, *110*, 042903.
[23] Y. J. Chen, S. Brahma, C. P. Liu, J.-L. Huang, *J. Alloys Compd.* **2017**, *728*, 1248.
[24] S. Goel, B. Kumar, *J. Alloys Compd.* **2020**, *816*, 152491.
[25] L. Meng, H. Chai, Z. Lv, T. Yang, *Opt. Express* **2021**, *29*, 11301.
[26] L. Meng, Z. Lv, H. Chai, X. Yang, T. Yang, *J. Phys. D: Appl. Phys.* **2022**, *55*, 19LT01.
[27] A. Ohtomo, M. Kawasaki, T. Koida, K. Masubuchi, H. Koinuma, Y. Sakurai, Y. Yoshida, T. Yasuda, Y. Segawa, *Appl. Phys. Lett.* **1998**, *72*, 2466.
[28] T. Makino, Y. Segawa, M. Kawasaki, A. Ohtomo, R. Shiroki, K. Tamura, T. Yasuda, H. Koinuma, *Appl. Phys. Lett.* **2001**, *78*, 1237.
[29] T. Maemoto, N. Ichiba, H. Ishii, S. Sasa, M. Inoue, *J. Phys.: Conf. Ser.* **2007**, *59*, 670.
[30] X. Yuan, T. Yamada, L. Meng, *Appl. Phys. Lett.* **2022**, *121*, 152903.
[31] K. Ferri, S. Bachu, W. Zhu, M. Imperatore, J. Hayden, N. Alem, N. Giebink, S. Trolier-McKinstry, J.-P. Maria, *J. Appl. Phys.* **2021**, *130*, 044101.
[32] S. Fichtner, N. Wolff, F. Lofink, L. Kienle, B. Wagner, *J. Appl. Phys.* **2019**, *125*, 114103.
[33] A. Konishi, T. Ogawa, C. A. J. Fisher, A. Kuwabara, T. Shimizu, S. Yasui, M. Itoh, H. Moriwake, *Appl. Phys. Lett.* **2016**, *109*, 102903.
[34] D. A. Scrymgeour, V. Gopalan, T. E. Haynes, *Integr. Ferroelectr.* **2001**, *41*, 35.

[35] D. A. Scrymgeour, A. Sharan, V. Gopalan, K. T. Gahagan, J. L. Casson, R. Sander, J. M. Robinson, F. Muhammad, P. Chandramani, F. Kiamilev, *Appl. Phys. Lett.* **2002**, *81*, 3140.
[36] S. Trolier-McKinstry, R. E. Newnham, *Materials Engineering: Bonding, Structure, and Structure-Property Relationships*, Cambridge University Press, Cambridge **2018**.
[37] V. Srikant, D. R. Clarke, *J. Appl. Phys.* **1998**, *83*, 5447.
[38] S. Heo, E. Cho, H.-I. Lee, G. S. Park, H. J. Kang, T. Nagatomi, P. Choi, B.-D. Choi, *AIP Adv.* **2015**, *5*, 077167.
[39] J. Tauc, R. Grigorovici, A. Vancu, *Phys. Status Solidi B* **1966**, *15*, 627.
[40] B. D. Viezbicke, S. Patel, B. E. Davis, D. P. Birnie III, *Phys. Status Solidi B* **2015**, *252*, 1700.
[41] S. A. Denev, T. T. A. Lummen, E. Barnes, A. Kumar, V. Gopalan, *J. Am. Ceram. Soc.* **2011**, *94*, 2699.
[42] N. Bloembergen, P. S. Pershan, *Phys. Rev.* **1962**, *128*, 606.
[43] W. N. Herman, L. M. Hayden, *J. Opt. Soc. Am. B* **1995**, *12*, 416.
[44] D. A. Kleinman, *Phys. Rev.* **1962**, *126*, 1977.
[45] R. C. Miller, *Appl. Phys. Lett.* **1964**, *5*, 17.
[46] M. C. Larciprete, M. Centini, *Appl. Phys. Rev.* **2015**, *2*, 031302.
[47] R. Zu, B. Wang, J. He, J.-J. Wang, L. Weber, L.-Q. Chen, V. Gopalan, *npj Comput. Mater.* **2022**, *8*, 246.
[48] G. Wang, G. T. Kiehne, G. K. L. Wong, J. B. Ketterson, X. Liu, R. P. H. Chang, *Appl. Phys. Lett.* **2002**, *80*, 401.
[49] F. Liang, L. Kang, Z. Lin, Y. Wu, *Cryst. Growth Des.* **2017**, *17*, 2254.
[50] D. N. Nikogosyan, *Nonlinear Optical Crystals: A Complete Survey*, Springer-Verlag, New York **2005**.
[51] M. Vallade, *Phys. Rev. B* **1975**, *12*, 3755.
[52] M. E. Lines, A. M. Glass, *Principles and Applications of Ferroelectrics and Related Materials*, Oxford University Press, Oxford, New York **2001**.
[53] K. Harun, N. Mansor, M. K. Yaakob, M. F. M. Taib, Z. A. Ahmad, A. A. Mohamad, *J. Sol-Gel Sci. Technol.* **2016**, *80*, 56.
[54] D. M. Hoat, V. V. On, D. Khanh Nguyen, M. Naseri, R. Ponce-Pérez, T. V. Vu, J. F. Rivas-Silva, N. N. Hieu, G. H. Cocoletzi, *RSC Adv.* **2020**, *10*, 40411.
[55] D. Damjanovic, *Rep. Prog. Phys.* **1998**, *61*, 1267.
[56] M. J. Haun, E. Furman, S. J. Jang, L. E. Cross, *Ferroelectrics* **1989**, *99*, 13.
[57] D. Damjanovic, *J. Am. Ceram. Soc.* **2005**, *88*, 2663.
[58] T. Zheng, J. Wu, D. Xiao, J. Zhu, *Prog. Mater. Sci.* **2018**, *98*, 552.
[59] M. J. Haun, E. Furman, S. J. Jang, L. E. Cross, *Ferroelectrics* **1989**, *99*, 63.
[60] D. Alden, W. Guo, R. Kirste, F. Kaess, I. Bryan, T. Troha, A. Bagal, P. Reddy, L. H. Hernandez-Balderrama, A. Franke, S. Mita, C.-H. Chang, A. Hoffmann, M. Zgonik, R. Collazo, Z. Sitar, *Appl. Phys. Lett.* **2016**, *108*, 261106.
[61] D. Alden, T. Troha, R. Kirste, S. Mita, Q. Guo, A. Hoffmann, M. Zgonik, R. Collazo, Z. Sitar, *Appl. Phys. Lett.* **2019**, *114*, 103504.
[62] J. Park, Y. Yamazaki, M. Iwanaga, H. Jeon, T. Fujiwara, T. Yao, *Opt. Express* **2010**, *18*, 7851.
[63] G. D. Boyd, C. K. N. Patel, *Appl. Phys. Lett.* **1966**, *8*, 313.
[64] P. Giannozzi, S. Baroni, N. Bonini, M. Calandra, R. Car, C. Cavazzoni, D. Ceresoli, G. L. Chiarotti, M. Cococcioni, I. Dabo, A. D. Corso, S. de Gironcoli, S. Fabris, G. Fratesi, R. Gebauer, U. Gerstmann, C. Gougoussis, A. Kokalj, M. Lazzeri, L. Martin-Samos, N. Marzari, F. Mauri, R. Mazzarello, S. Paolini, A. Pasquarello, L. Paulatto, C. Sbraccia, S. Scandolo, G. Sclauzero, A. P. Seitsonen, et al., *J. Phys.: Condens. Matter* **2009**, *21*, 395502.
[65] P. Giannozzi, O. Andreussi, T. Brumme, O. Bunau, M. B. Nardelli, M. Calandra, R. Car, C. Cavazzoni, D. Ceresoli, M. Cococcioni, N. Colonna, I. Carnimeo, A. D. Corso, S. de Gironcoli, P. Delugas, R. A. DiStasio, A. Ferretti, A. Floris, G. Fratesi, G. Fugallo, R. Gebauer, U. Gerstmann, F. Giustino, T. Gorni, J. Jia, M. Kawamura, H.-Y. Ko, A. Kokalj, E. Küçükbenli, M. Lazzeri, et al., *J. Phys.: Condens. Matter* **2017**, *29*, 465901.
[66] M. J. van Setten, M. Giantomassi, E. Bousquet, M. J. Verstraete, D. R. Hamann, X. Gonze, G.-M. Rignanese, *Comput. Phys. Commun.* **2018**, *226*, 39.
[67] K. Lejaeghere, G. Bihlmayer, T. Björkman, P. Blaha, S. Blügel, V. Blum, D. Caliste, I. E. Castelli, S. J. Clark, A. Dal Corso, S. de Gironcoli, T. Deutsch, J. K. Dewhurst, I. Di Marco, C. Draxl, M. Dułak, O. Eriksson, J. A. Flores-Livas, K. F. Garrity, L. Genovese, P. Giannozzi, M. Giantomassi, S. Goedecker, X. Gonze, O. Grånäs, E. K. U. Gross, A. Gulans, F. Gygi, D. R. Hamann, P. J. Hasnip, et al., *Science* **2016**, *351*, aad3000.
[68] D. R. Hamann, *Phys. Rev. B* **2013**, *88*, 085117.
[69] J. P. Perdew, J. A. Chevary, S. H. Vosko, K. A. Jackson, M. R. Pederson, D. J. Singh, C. Fiolhais, *Phys. Rev. B* **1992**, *46*, 6671.
[70] A. D. Becke, *Phys. Rev. A* **1988**, *38*, 3098.
[71] D. C. Langreth, M. J. Mehl, *Phys. Rev. B* **1983**, *28*, 1809.
[72] J. P. Perdew, K. Burke, M. Ernzerhof, *Phys. Rev. Lett.* **1996**, *77*, 3865.
[73] A. H. Larsen, J. J. Mortensen, J. Blomqvist, I. E. Castelli, R. Christensen, M. Dułak, J. Friis, M. N. Groves, B. Hammer, C. Hargus, E. D. Hermes, P. C. Jennings, P. B. Jensen, J. Kermode, J. R. Kitchin, E. L. Kolsbjerg, J. Kubal, K. Kaasbjerg, S. Lysgaard, J. B. Maronsson, T. Maxson, T. Olsen, L. Pastewka, A. Peterson, C. Rostgaard, J. Schiøtz, O. Schütt, M. Strange, K. S. Thygesen, T. Vegge, et al., *J. Phys.: Condens. Matter* **2017**, *29*, 273002.
[74] I. Timrov, N. Marzari, M. Cococcioni, *Phys. Rev. B* **2018**, *98*, 085127.
[75] I. Timrov, N. Marzari, M. Cococcioni, *Comput. Phys. Commun.* **2022**, *279*, 108455.
[76] N. E. Kirchner-Hall, W. Zhao, Y. Xiong, I. Timrov, I. Dabo, *Appl. Sci.* **2021**, *11*, 2395.
[77] S. Baroni, S. de Gironcoli, A. Dal Corso, P. Giannozzi, *Rev. Mod. Phys.* **2001**, *73*, 515.
[78] R. Resta, D. Vanderbilt, in *Physics of Ferroelectrics: A Modern Perspective*, Springer, Berlin, Heidelberg **2007**, pp. 31–68.
[79] N. A. Spaldin, *J. Solid State Chem.* **2012**, *195*, 2.
[80] S. Jesse, S. V. Kalinin, R. Proksch, A. P. Baddorf, B. J. Rodriguez, *Nanotechnology* **2007**, *18*, 435503.